Available online at www.sciencedirect.com
SCIENCE DIRECT®
ELSEVIER
Journal of Magnetism and Magnetic Materials 293 (2005) 677–684
Journal of magnetism and magnetic materials
www.elsevier.com/locate/jmmm

Magnetic microbead detection using the planar Hall effect

Louise Ejsing[a,*], Mikkel F. Hansen[a], Aric K. Menon[a], Hugo A. Ferreira[b], Daniel L. Graham[b], Paulo P. Freitas[b]

[a]*Department of Micro and Nanotechnology (MIC), Technical University of Denmark (DTU), Building 345 east, DK-2800 Kongens Lyngby, Denmark*
[b]*Institute of Engineering of Systems and Computers—Microsystems and Nanotechnologies (INESC-MN), Rua Alves Redol 9, Lisbon 1000-029, Portugal*

Available online 29 March 2005

Abstract

Magnetic sensors based on the planar Hall effect of exchanged-biased permalloy have been fabricated and characterized. It is demonstrated that the sensors are feasible for detecting just a few commercial 2.0 μm magnetic beads commonly used for bioseparation (Micromer-M, Micromod, Germany) and that the sensor sense current is sufficient to generate a signal from the beads.
© 2005 Elsevier B.V. All rights reserved.

PACS: 75; 47; −m

Keywords: Hall effect (planar); Micromer-M; Magnetic sensor; Biosensor; Permalloy ($Ni_{80}Fe_{20}$); MnIr ($Mn_{76}Ir_{24}$); Detection of microspheres

1. Introduction

In the lab-on-a-chip concept all steps in analyzing a sample are assembled on a single chip. The idea is to use such a chip directly after taking, e.g., a blood sample to obtain an immediate answer as to the presence of a specific molecule. Our focus has been on the detection step, where we aim to use magnetic beads and integrate bead detection with microfluidic channels.

Detection of superparamagnetic beads for biosensor applications has been demonstrated using GMR sensors [1–3], spin valve sensors [4–7], and a silicon Hall sensor [8]. Planar Hall effect sensors have been shown to exhibit nano-Tesla sensitivity [9,10] and have recently been investigated for their use in magnetic biodetection [11]. We propose the use of microfabricated planar Hall effect (PHE) sensors and demonstrate bead detection in zero externally applied field using an exchange-biased permalloy sensor. This sensor is significantly

*Corresponding author. Tel.: +45 4525 6336; fax: +45 4588 7762.
E-mail address: loe@mic.dtu.dk (L. Ejsing).

0304-8853/$ - see front matter © 2005 Elsevier B.V. All rights reserved.
doi:10.1016/j.jmmm.2005.02.071

improved compared to the unbiased nickel PHE sensor previously demonstrated [11].

The purpose of exchange-biasing the sensor is to ensure a sufficient uniaxial anisotropy, a well-defined single domain state and to introduce a unidirectional anisotropy. The sign of the sensor output depends upon whether the film magnetization is initially parallel or antiparallel to the sensor current (Section 2) and thus it is important to have a well-defined initial orientation. For the previously demonstrated Ni sensor, which exhibited uniaxial anisotropy, this was achieved by saturating the sensor along one of the easy directions prior to each measurement. Due to the unidirectional anisotropy this step is now eliminated and, additionally, the higher anisotropic magnetoresistance of permalloy compared to Ni results in a larger signal.

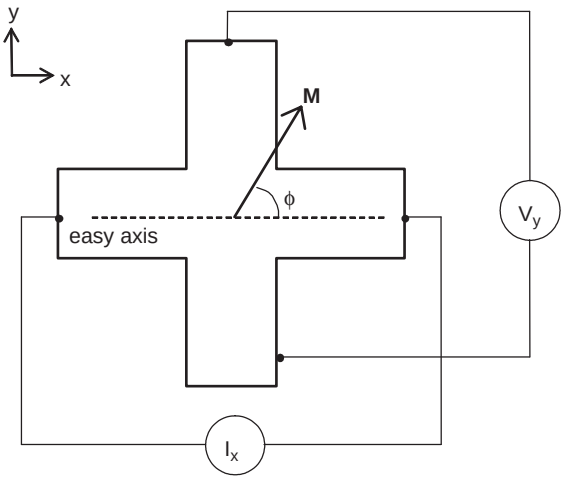

Fig. 1. Planar Hall geometry. A current is applied in the x-direction and a voltage is measured in the y-direction. The magnetization vector, $\mathbf{M}$, lies in the x–y-plane at an angle, ϕ, to the current direction. The easy axis is along the current direction.

2. Planar Hall effect sensor principle

The magnetic sensor is based on the anisotropic magnetoresistance of ferromagnetic materials. For such materials, Ohm's law can be written [12]

$$\vec{\mathbf{E}} = \hat{\mathbf{M}}(\mathbf{J}\cdot\hat{\mathbf{M}})[\rho_{||}-\rho_{\perp}] + \rho_{\perp}\mathbf{J} + \rho_{\mathrm{H}}\hat{\mathbf{M}}\times\mathbf{J}, \qquad (1)$$

where $\hat{\mathbf{M}}$ denotes a unit vector along the magnetization direction and $\mathbf{J}$ is the current density. ρ_{H} is the ordinary Hall resistivity arising from the Lorentz force deflection of the charge carriers. $\rho_{||}$ and $\rho_{\perp}$ are the resistivities when the magnetization vector is parallel and perpendicular to the current density, respectively. Generally, $\rho_{||} > \rho_{\perp}$ and for Ni–Fe alloys $\Delta\rho\cdot\rho_{\mathrm{av}}^{-1} \equiv (\rho_{||}-\rho_{\perp})\cdot\rho_{\mathrm{av}}^{-1}$ attains values up to 3% at room temperature [13]. A sensor based on the planar Hall geometry illustrated in Fig. 1 can be used for detection of small magnetic fields [9–11,14]. The sensor consists of a thin ferromagnetic film through which a current I_x is applied in the x-direction and the voltage V_y is measured in the y-direction. The magnetization vector lies in the plane of the sensor at an angle ϕ to the current direction. For this geometry Eq. (1) reduces to

$$E_y = (\rho_{||}-\rho_{\perp})J_x\sin\phi\cos\phi \qquad (2)$$

and the measured voltage becomes

$$V_y = \tfrac{1}{2}I_x\Delta R\sin(2\phi), \qquad (3)$$

where $\Delta R \equiv (\rho_{||}-\rho_{\perp})\cdot t_{\mathrm{film}}^{-1}$ and t_{film} is the film thickness. The basic principle of the sensor is the following. The easy axis and the easy direction of magnetization are defined in the film along the current direction by exchange-coupling to an antiferromagnetic material. If a magnetic field is subsequently applied perpendicular to the easy axis the magnetization vector rotates away from the easy direction, giving rise to an electrical response according to Eq. (3). To model the sensor response, we can to a first approximation write the magnetic energy density of the film as

$$U = K_{\mathrm{u}}\sin^2\phi - U_{\mathrm{E}}\cos\phi - \mu_0 M H_y\sin\phi, \qquad (4)$$

where K_{u} is the uniaxial anisotropy constant, U_{E} is the exchange energy density, and H_y is the magnetic field affecting the sensor along the y-direction. For small angles, $\cos\phi \approx 1$, and minimization of the energy yields

$$\sin\phi \approx \frac{\mu_0 M H_y}{2K_{\mathrm{u}}+U_{\mathrm{E}}} \equiv \frac{H_y}{H_{\mathrm{C}}+H_{\mathrm{E}}}, \qquad (5)$$

which is valid for $H_y \ll H_C + H_E$. H_C is the anisotropy field, and H_E is the exchange coupling field. Insertion in Eq. (3) yields the ideal sensor response

$$V_y \approx I_x \Delta R \frac{H_y}{H_C + H_E}. \quad (6)$$

The expected sensor response, plotted in Fig. 2, is linear to within 2% for $|H_y(H_C + H_E)^{-1}| < 0.2$ with the sensitivity

$$S_0 \equiv \frac{V_y}{H_y I_x} = \frac{\Delta R}{H_C + H_E}. \quad (7)$$

The PHE magnetic sensor is sensitive to magnetic fields in the sensor plane. This is utilized to detect the dipole field from magnetic beads as illustrated in Fig. 3. The applied magnetic field magnetizes the bead and creates a dipole field, which is antiparallel to the applied field in the sensor plane. Thus, the presence of magnetic beads gives rise to a reduction of the applied field, which can be detected.

The magnetic beads contain superparamagnetic nanoparticle inclusions and will show a linear response at low fields. Hence, the bead magnetization can be written $\mathbf{M} = \chi\mathbf{H}$, where χ is the bead susceptibility (including demagnetization effects) and $\mathbf{H}$ is the field intensity containing contributions from the applied field, the field generated by

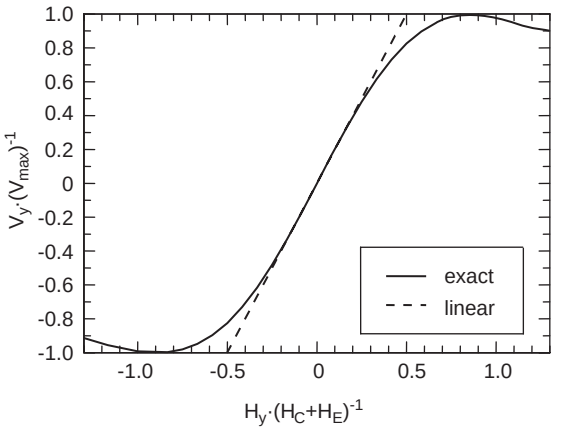

Fig. 2. Expected ideal sensor response as a function of applied magnetic field strength. The dotted line shows the approximation of Eq. (6) $V \propto H_y \cdot (H_C + H_E)^{-1}$.

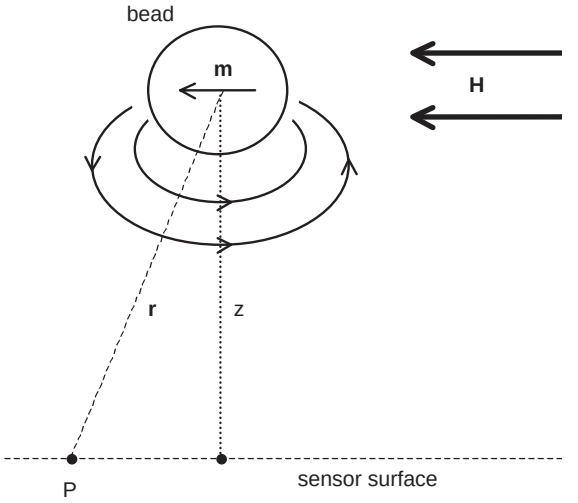

Fig. 3. Magnetic bead with moment, **m**, positioned relative to the sensor surface. The bead is magnetized in the field, **H**, and produces a field in the opposite direction at the sensor.

the current through the sensor, the field from other beads, and possibly the fringing field from the sensor itself. It will be assumed below that **H** is essentially in the y-direction. The magnetic field outside a homogeneously magnetized sphere is identical to the dipole field

$$\mathbf{H}_{dip} = \frac{m}{4\pi r^3}(3\hat{\mathbf{r}}(\hat{\mathbf{m}} \cdot \hat{\mathbf{r}}) - \hat{\mathbf{m}}), \quad (8)$$

where $\hat{}$ denotes unit vectors, $\mathbf{r} = r\hat{\mathbf{r}}$ is a vector connecting the centre of the bead to a point P on the sensor, $\mathbf{m} = \chi V_{bead}\mathbf{H}$ is the bead moment and V_{bead} is the bead volume. From this, a crude estimate of the order of magnitude of the dipole field experienced by the sensor is $\sim -\mathbf{H}\chi V_{bead}(4\pi z^3)^{-1}$, where z is the normal distance between the centre of the bead and the sensor surface. The error made by this assumption becomes smaller when the sensor dimension becomes comparable to or smaller than z. Defining the influenced area, A_{bead}, of the sensor as the cross-section of the bead and averaging the dipole field over the entire sensor surface, one can find that the crude estimate given above should be multiplied by a factor 0.38 to be correct [15]. Thus, defining the fraction of the sensor area influenced by the bead as $f = A_{bead}/A_{sensor}$, the total field

experienced by the sensor from N independently acting beads is

$$H_y \approx H_{\text{app}} - \frac{0.38 f N H \chi V_{\text{bead}}}{4\pi z^3}, \tag{9}$$

where H_{app} is the applied external field and it is reminded that H is the total magnetic field on a bead in the y-direction. Hence, the presence of the beads reduce the effective sensitivity of the sensor to an external field by a number proportional to the number of beads and the voltage drop over the sensor is estimated to

$$V_y = S_0 H_y I_x \approx V_0 \left(1 - \frac{H}{H_{\text{app}}} \frac{0.38 f N \chi V_{\text{bead}}}{4\pi z^3}\right), \tag{10}$$

where $V_0 = S_0 H_{\text{app}} I_x$.

3. Sensor fabrication and characterization

The PHE sensors are fabricated using conventional clean room fabrication methods. The sensor layer structure of Ta(30 Å)–NiFe(50 Å)–MnIr(200 Å)–NiFe(200 Å)–Ta(30 Å), presented in Fig. 4, is deposited by ion beam deposition on top of a 3″ silicon wafer passivated by Al_2O_3, and a TiWN(150 Å) anti-reflecting layer is sputtered on top. The 50 Å NiFe layer is included to ensure proper growth conditions for the following MnIr layer. For ion beam deposition conditions see Gehanno et al. [13]. Here, MnIr stands for $Mn_{76}Ir_{24}$ and NiFe stands for $Ni_{80}Fe_{20}$. During ion beam deposition a homogeneous magnetic field of 40 Oe is applied in order to form an easy magnetic direction. The sensors are patterned by direct laser writing into photoresist and the excess material is ion-milled away in a physical dry-etch. Current leads and bonding pads of 0.3 μm thick Al are defined in final lithography, physical vapour deposition, and lift-off steps. The whole wafer is then passivated by 0.2 μm sputtered SiO_2, and the contact pads are opened by reactive ion etching. Finally, the wafer is diced and wire bonded to the electrical contacts.

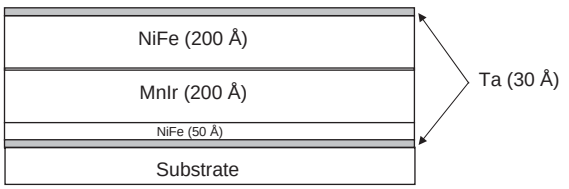

Fig. 4. Sensor material layer structure. The bottom Ta(30 Å) layer is for adhesion and epitaxial growth of NiFe(50 Å), which ensures epitaxial growth of the antiferromagnetic MnIr(200 Å), which pins the sensor layer of NiFe(200 Å), top Ta(30 Å) hinders corrosion.

Fig. 5 shows a micrograph of a sensor. A dotted frame indicates the sensitive area of the sensor, but beads from the vicinity can contribute to the signal with reduced magnitude according to the r^{-3} dependence of the dipole field.

Fig. 6 shows vibrating sample magnetometer data obtained on a continuous film of the stack measured with the applied field along the deposition field. It is seen that the hysteresis loop essentially consists of two hysteretic signals, one accounting for ≈83% of the film moment with $H_E = 41$ Oe and $H_C = 18$ Oe and another accounting for ≈17% of the film moment with $H_E = 274$ Oe and $H_C = 21$ Oe. The two signals are attributed to the 200 and 50 Å NiFe layers, respectively. In addition, there is a small hysteretic

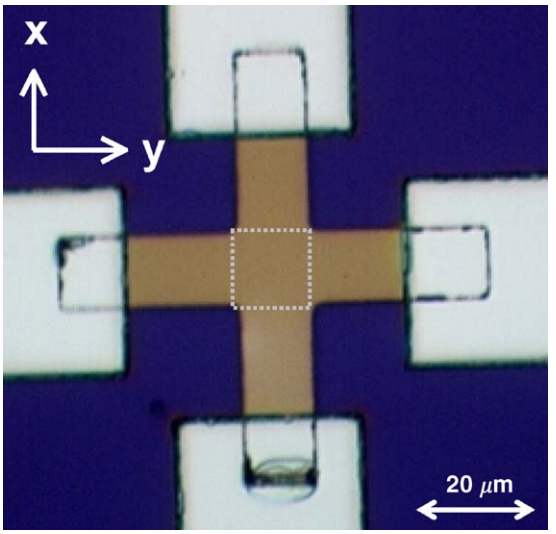

Fig. 5. Top view micrograph of the planar Hall sensor. The cross is made of magnetic layers (see layer structure in Fig. 4), and the central area marked by a dotted frame is the 10 μm × 10 μm sensitive area of the sensor. Current leads are made of 0.3 μm thick Al.

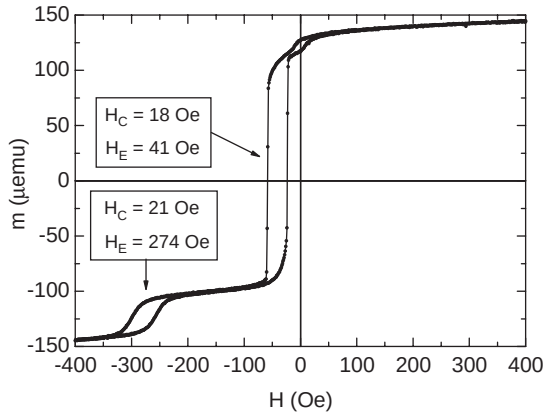

Fig. 6. Vibrating sample magnetometer data on the exchange-biased permalloy film (see Fig. 4 for details on the material structure) measured with the applied field along the easy direction.

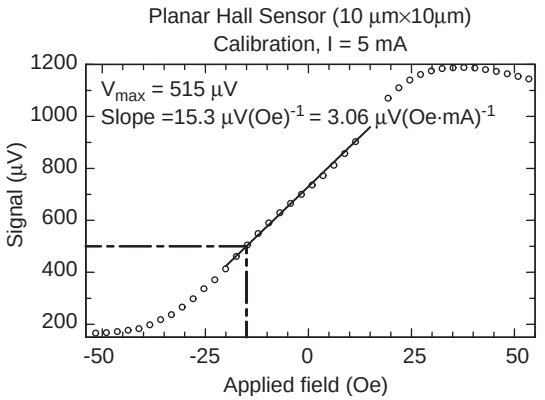

Fig. 7. Calibration curve for the planar Hall effect sensor. $V_{\max}$ is the highest signal minus the offset value at $H = 0$ Oe, but the curve is shifted from $H = 0$ Oe due to a remanent magnetization of the coil used to produce the applied field. Hence, $V_{\max}$ is measured as $\frac{1}{2}\times$peak-to-peak signal. The slope of the linear region gives the sensitivity of the sensor as $S = 3.06\,\mu\text{V(Oe mA)}^{-1}$ linear to within 2.8%. At $H = -15$ Oe, $V_y = 500\,\mu$V.

impurity near zero field of unknown origin. Note the enhancement of the coercive field with respect to that of unbiased permalloy and that the value of $H_E + H_C$ to enter in Eq. (7) for the 200 Å biased permalloy layer is 59 Oe. This layer is expected to dominate the electrical response of the sensor.

The electrical characterization of the PHE sensors was carried out by measuring the DC sensor response using a digital multimeter as function of the magnetic field provided by electromagnetic coils. The sensor voltage measured for fields between $\approx \pm 50$ Oe for a sensing current $I_x = 5$ mA is shown in Fig. 7. It is seen that there is a significant additional voltage offset due to, e.g., imperfections of the lithographic process and a small field offset due to a remanent field of the electromagnet. Though present throughout the measurements, the voltage offset does not influence the sensitivity of the PHE sensor and is hence subtracted from the following results. It is seen that the general trend of the signal is in agreement with that expected from the simple theory (Fig. 2). The low-field part of the curve (between $+15$ and -20 Oe applied field strength) is linear to within 2.8% with a slope of $S_0 = 3.06\,\mu\text{V(Oe mA)}^{-1}$. The slope is reproducible both for the particular sensor and for all sensors on the same wafer. Table 1 summarizes the experimental characteristics of the sensor and the theoretical predictions for comparison. In the theoretical estimates of R_{DC} and the AMR, based on the values for AMR of NiFe and resistivities found in [13], shunting of the current through the other layers is taken into account. For the estimate of $V_{\max}$ and the slope, only the NiFe(200 Å) layer is considered; though the NiFe(50 Å) might affect the signal, its contribution should be much smaller than that from the thick layer.

Table 1
Experimental and theoretical values for sensor calibration

Property	Experimental	Theoretical
R_{DC}	51.9 Ω	25 Ω
AMR ($\Delta R \cdot R^{-1}$)	1.3%	1.9%
$V_{\max}$ (Eq. (3) for $\varphi = \pi/4$)	515 μV	458 μV
$H(V = V_{\max})$	44 Oe	47 Oe
S_0	$3.06\,\mu\text{V(Oe mA)}^{-1}$	$3.86\,\mu\text{V(Oe mA)}^{-1}$

4. Detection of magnetic beads

In a recent paper [16], we have demonstrated that the present sensors are feasible for the

detection of commercial 2 μm Micromer-M and 250 nm Nanomag-D magnetic beads (Micromod, Germany [17]). These experiments were performed by measuring the voltage drop across the sensor while droplets containing magnetic beads were introduced to the sensor and subsequently washed off. A sensing current of 10 mA and an applied external field of −15 Oe were used. From a comparison of a direct counting of beads flowing by the sensor under an optical microscope with the corresponding sensor signals, it was estimated that each 2 μm Micromer-M bead contributed with a signal of ~0.3 μV. The corresponding noise level of the unshielded DC measurements was of the same magnitude.

Here, we present experiments on the detection of 2 μm Micromer-M beads with and without applying an external field from the electromagnetic coils of −15 Oe. The properties of the Micromer-M beads are summarized in Table 2. A bead magnetized by −15 Oe gives rise to a field just below the bead of +1.5 Oe. The contribution to the field outside the sensor from the sensing current can be estimated using Ampère's law to

$$H_{\text{sense}}(z) \approx \frac{I_x}{2w + 2\pi z}, \tag{11}$$

where w is the width of the current line. At $z =$ 1.5 μm, which is a typical value for the first layer of 2 μm beads, this field amounts to ≈0.4 Oe per mA applied sensing current.

Fig. 8 shows an example of a bead detection experiment performed in an applied field of −15 Oe. The current applied to the sensor is $I_x =$ 15 mA giving rise to an estimated field of 6 Oe from the sensing current at the first monolayer of beads. At time $t = 250$ s beads are added and the signal changes as the beads settle on top of the sensor, at time $t = 550$ s the beads are washed off the sensor and the signal returns to its previous value. At times $t = 750$ and 1025 s, respectively, the experiment is repeated yielding the same result though with a little higher saturation signal. An estimate of the sensor coverage assuming that the dipole fields from the beads are independent and that the beads are close packed on the sensor surface yields ≈1.5 monolayers. The electrical noise level of the measurement is ≈250 nV.

Table 2
Physical properties of Micromer-M beads [16]

Micromer-M beads	
Diameter	2 μm
Concentration	$>25\,\text{mg ml}^{-1}$
Density (ρ)	$1.4\,\text{g cm}^{-3}$
χ (measured at INESC-MN)	0.3 ± 0.1 [SI]

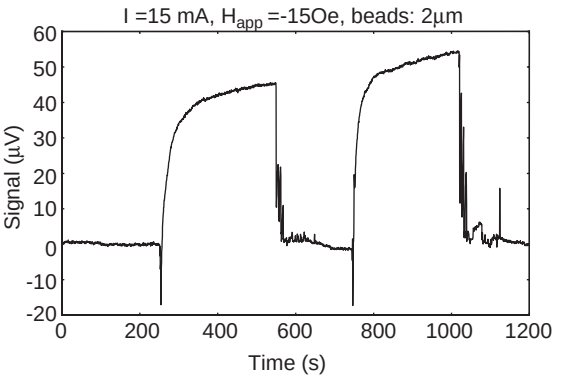

Fig. 8. Bead detection in an applied field, $H_{\text{app}} = -15$ Oe and a sensing current of $I_x = 15$ mA. A voltage offset of 1483 μV is subtracted. At times $t = 250$ and 750 s the beads are added onto the chip, and the signal changes according to Eq. (10) until it reaches a saturation value. At times $t = 550$ and 1025 s the beads are washed off the sensor, and the signal returns to the baseline.

Fig. 9 shows detection measurements of beads without applying a magnetic field. The current through the sensor, $I_x = 10$ mA, corresponds to a field 1.5 μm above the sensor of ≈4 Oe. At time $t = 580$ s a dilute bead solution is added to the chip and at time $t = 660$ s the beads are washed off the sensor. At times $t = 675$ and 795 s groups of beads are observed on top of the sensitive area. The first group constitutes two beads, the other four beads. They are removed by flushing with water at times $t = 700$ and 810 s, respectively. At time $t = 840$ s a concentrated solution of beads is added to the chip and the signal saturates at approximately $V =$ 30 μV, then the beads are removed between $t =$ 920 and 950 s and the signal returns to its baseline. The electrical noise level of the measurement is ≈250 nV.

These measurements show that the magnetic field generated from the sensing current is

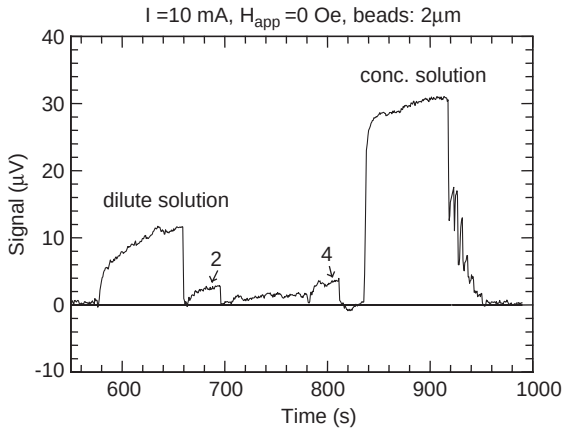

Fig. 9. Bead detection in zero applied field, $H_{app} = 0$ Oe and a sensing current of $I_x = 10$ mA. A voltage offset of 1775 μV is subtracted. The sensor senses a diluted bead solution, then few beads (2 and 4), and a concentrated bead solution with a saturation signal of $V = 30$ μV.

sufficient to yield a significant response from the beads. Due to the inhomogeneous nature of this field, it will also assist in the collection of beads on top of the sensor. The fact, that the peaks for two and four beads are clearly distinguishable indicates that the sensors are feasible for the detection of a few beads or a single bead even in the absence of an externally applied magnetizing field. It is noted that the noise level of the unshielded DC measurements is expected to be improved significantly by use of lock-in technique. Although the sensor signal of PHE sensors is lower compared to equivalent spin valve and GMR sensors, the $1/f$ dominated low-frequency noise level is even lower due to the higher number of charge carriers such that the signal-to-noise ratio turns out to be a factor of 3–4 higher [15]. Thus, PHE sensors are promising candidates for the detection of single magnetic beads with diameters well below 1 μm.

Similar experiments have been carried out for a number of sensing currents between 5 and 15 mA and an analysis of the sensor response and estimates of the number of beads collected on the sensor using Eq. (10) with the magnetizing field given by Eq. (11) yield roughly a constant coverage of 1.4 monolayers and no clear dependence on the applied sensing current is observed. This is likely due to the rather high initial concentration of beads in the fluid such that the sensor is essentially saturated with beads and that the addition of more beads does not lead to a significant signal increase due to the r^{-3} decay of the dipole field from the beads. Also, it is difficult to exactly repeat experimental conditions (fluid amounts, settle times, number of beads, etc.) from one experiment to the next. Experiments on systems integrated with microfluidic channels with very dilute bead solutions and a constant fluid flow will probably aid in the clarification of the contribution of the sensing current to the capture efficiency and bead signal.

5. Conclusion

The planar Hall effect sensor is demonstrated capable of detecting the presence of 2 μm Micromer-M beads. These beads are used for attaching biomolecules in biological applications such as biosensing, separation and purification protocols. The bead surfaces are covered with streptavidin to enable binding of DNA or proteins. Hence, with a suitable biochemical coating of the sensor surface, the planar Hall effect sensor can detect the presence of DNA or proteins via the presence of the magnetic bead. The sensor is demonstrated sensitive enough to detect very few beads. Due to the simple fabrication scheme, the planar Hall sensor can be easily integrated into lab-on-a-chip systems, and the demonstration of bead detection in the field generated by the sensing current, i.e., without applying external fields, is promising for chip integration.

Due to the cross geometry, the planar Hall effect sensor uses its entire active surface for bead and biomolecule detection, which is not the case for meandering-type GMR or spin valve sensors. In addition, the sensing geometry, compared with the ordinary Hall sensor, utilizes all the magnitude of the magnetic dipole field induced by the bead. Another advantage, not exploited here, is that the theoretical signal-to-noise ratio of planar Hall effect sensors is higher than those of corresponding GMR and spin-valve sensors [15].

Future work includes demonstration of the planar Hall effect sensor as a biosensor, and

integration with fluidic biochips. Another prospect is to demonstrate detection of single nanometer-sized beads.

References

[1] D.R. Baselt, G.U. Lee, M. Natesan, et al., Biosensors Bioelectron. 13 (1998) 731.
[2] R.L. Edelstein, C.R. Tamanaha, P.E. Sheehan, et al., Biosensors Bioelectron. 14 (2000) 805.
[3] M.M. Miller, P.E. Sheehan, R.L. Edelstein, et al., J. Magn. Magn. Mater. 225 (2001) 138.
[4] D.L. Graham, H. Ferreira, J. Bernardo, et al., J. Appl. Phys. 91 (2002) 7786.
[5] H.A. Ferreira, D.L. Graham, P.P. Freitas, et al., J. Appl. Phys. 93 (2003) 7281.
[6] D.L. Graham, H.A. Ferreira, P.P. Freitas, et al., Biosensors Bioelectron. 18 (2003) 483.
[7] G. Li, V. Joshi, R.L. White, et al., J. Appl. Phys. 93 (2003) 7557.
[8] P.-A. Besse, G. Boero, M. Demierre, et al., Appl. Phys. Lett. 80 (2002) 4199.
[9] F. Montaigne, A. Schuhl, F.N. Van Dau, et al., Sensors Actuators 81 (2000) 324.
[10] F.N. Van Dau, A. Schuhl, J.R. Childress, et al., Sensors Actuators A 53 (1996) 256.
[11] L. Ejsing, M.F. Hansen, A.K. Menon, Planar Hall effect magnetic sensor for microbead detection, Extended Abstract, Eurosensors 2003, 2003, p. 1095.
[12] R.C. O'Handley, Modern Magnetic Materials, Wiley, New York, 2000.
[13] V. Gehanno, P.P. Freitas, A. Veloso, et al., IEEE Trans. Magn. 35 (1999) 4361.
[14] A. Schuhl, F.N. Van Dau, J.R. Childress, Appl. Phys. Lett. 66 (1995) 2751.
[15] P.P. Freitas, H.A. Ferreira, D.L. Graham, et al., in: M. Johnson (Ed.), Magnetoresistive Biochips, Elsevier, Amsterdam, 2004.
[16] L. Ejsing, M.F. Hansen, A.K. Menon, et al., Appl. Phys. Lett. 84 (2004) 4729.
[17] http://www.micromod.de.